Evidence of separator reconnection in a survey of X-ray bright points

D.W. Longcope, C.C. Kankelborg, J.L. Nelson and A.A. Pevtsov[1]
Department of Physics, Montana State University,
Bozeman, MT 59717

ABSTRACT

X-ray bright points are among the simplest coronal structures hypothesized to be powered by magnetic reconnection. Their magnetic field appears to consist of a simple loop of field lines connecting positive to negative photospheric sources. Quantitative three-dimensional models of reconnection in this geometry are therefore expected to apply directly to X-ray bright points. We assemble a survey from archival SOHO data of 764 X-ray bright points (EIT) along with their associated photospheric magnetic fields (SOI/MDI). Measurements are made of each quantity relevant to the simple three-dimensional reconnection model. These data support several predictions of a magnetic reconnection model providing further evidence in favor of the hypothesis that magnetic reconnection supplies heating power to the quiet solar corona.

1. Introduction

An X-ray bright point (XBP) is a small ($\lesssim$ 40 Mm) isolated feature apparent in Soft X-ray (Krieger, Vaiana, & van Speybroeck 1971, Golub et al. 1974) and EUV (Habbal & Withbroe 1981, Kankelborg et al. 1996) emission. X-ray bright points are found both in coronal holes and regions of quiet sun. In the vast majority of cases magnetograms show a small magnetic bipole (isolated sources of positive and negative flux in the photosphere) closely associated with the XBP (Golub et al. 1977). When their motion can be measured, a majority of XBP bipoles are found to be converging (Harvey et al. 1994, Webb et al. 1993), presumably destined to fully or partially cancel with one another (Harvey et al. 1999). During a typical eight-hour XBP life-time, X-ray and EUV emission can vary significantly, sometimes exhibiting brief "flares" (Nolte, Solodyna, & Gerassimenko 1979, Habbal, Dowdy, & Withbroe 1990, Strong et al. 1992).

[1]Present address: National Solar Observatory/Sacramento Peak, PO Box 62, Sunspot, NM 88349

The prevailing interpretation of these observational facts has been that XBPs result from reconnection in the magnetic field of the bipole. Since magnetograms typically show well-separated photospheric sources the magnetic reconnection probably takes place in the corona. Reconnection presumably releases magnetic energy in the corona, evaporating chromospheric material, either by precipitating electrons or by thermal conduction, thereby increasing the emission measure in the post-reconnection field lines (Habbal, Dowdy, & Withbroe 1990, Kankelborg et al. 1996). Observed variations in emission on time-scales much shorter than observed photospheric motion, such as in flares, suggests a reconnection process which is unsteady.

As a means of studying magnetic reconnection, XBPs offer several clear advantages over other reconnection-powered phenomena such as solar flares. First of all, the emitting plasma appears to constitute a few coronal loops – a loop is a system for which models exist (Rosner, Tucker, & Vaiana 1978, Vesecky, Antiochos, & Underwood 1979, Fisher & Hawley 1990) and engender a high degree of confidence. Secondly, the magnetic geometry in which the loop is embedded, a simple magnetic bipole, appears far simpler than the geometries of even so-called bipolar active regions. The only challenging aspect of the XBP scenario is the reconnection itself. In particular, how rapidly does magnetic field dissipate energy to power the bright point? We seek to answer this question by collecting a dataset, or survey, of X-ray bright points and associated bipoles from archival SOHO observations.

Comprehensive models of reconnecting bipoles have recently been developed in two (Priest, Parnell, & Martin 1994) and three dimensions (Parnell, Priest, & Golub 1994, Longcope 1998). Of these, the minimum current corona (MCC) model of Longcope (1998) uses several measurable quantities, and a few free parameters, to make quantitative predictions of morphology and power loss in a single XBP. The approach we adopt in this study is to measure those same quantities in the XBP/bipole data from our archival survey. This produces a readily manageable dataset and allows a direct application of the MCC.

At its most basic level the MCC proposes that power is supplied by reconnection of overlying or background field into the magnetic bipole. This reconnection happens at a point *between* the bipole field and the background, so the field lines which are most directly heated have properties intermediate between the two. For contrast we introduce a simpler picture, termed here the *naive bipole model*, where the XBP is a simple loop connecting the two poles along a direct path, heated by an unspecified *internal* mechanism. By fiat the naive model predicts a loop whose properties are defined by the bipole alone. We will seek evidence in the survey to support either the MCC or the naive bipole model.

Data from the Michelson Doppler Imager (MDI; Scherrer et al. 1995) on SOHO is used to calculate the parameters for each magnetic bipole. Placed in the MCC model these yield predictions of morphology and power loss in the associated XBP. All of the predicted quantities are also measured using data from the EUV Imaging Telescope (EIT; Delaboudiniere et al. 1995). The free parameters in the MCC characterize magnetic reconnection itself. Varying these to best match the model predictions to the data provides quantitative measurements about magnetic reconnection in the solar corona.

In this work we describe our archival survey and present its several results. We begin with a brief review, in §2, of the MCC model for a magnetic bipole. Section 3 presents the design of our survey, and describes the dataset we accumulated. Section 4 presents the method for calculating model parameters from MDI data, and predicted quantities from EIT data. Section 5 then describes the comparison of model predictions to measured data.

2. The MCC model for a bipole

A bipole consists of one positive and one negative photospheric source with magnetic fluxes Φ_+ and Φ_- respectively. These sources, P and N, are separated by a distance d along an axis $\mathbf{\Delta}$, from P to N, making an angle $\phi_{\rm bp}$ from heliographic West (see fig. 1a). The separation $d = |\mathbf{\Delta}|$ is assumed to be much greater than the photospheric diameter of either source, making them approximately point sources of magnetic flux. The point midway between the sources, $\bar{\mathbf{x}}_{\rm bp}$, will be used to define the location of the bipole.

In general, only some of the coronal field lines from P will connect to N (see fig. 1c). The remainder join a "background" magnetic field overlying the bipole, which is created by more distant poles and by active regions. For simplicity we model the background as a uniform horizontal field of strength B_0, directed at angle ϕ_0, as shown in fig. 1a. As the poles converge (diverge) they will seek to share more (less) magnetic flux with one another. They can only change their shared flux by reconnection with the background field. Figure 1c – 1d shows how this reconnection proceeds. Initially field lines connect P to the background and the background to N (fig. 1c). The process of magnetic reconnection can be visualized as cutting pairs of field lines and splicing them back together with a new set of connections. Figure 1d shows the field lines which result, some connect P to N, while others are part of the overlying background proper. The cutting and pasting occurs at or near that unique field line, called *the separator*, which lies at the interface of all four types of field lines. Only field lines connecting P to N pass beneath the separator.

A detailed quantitative theory of this process was presented by Longcope (1998). For present purposes, however, we derive its principal results on purely dimensional grounds, based on only two assumptions. First we assume that the internal structure of the sources

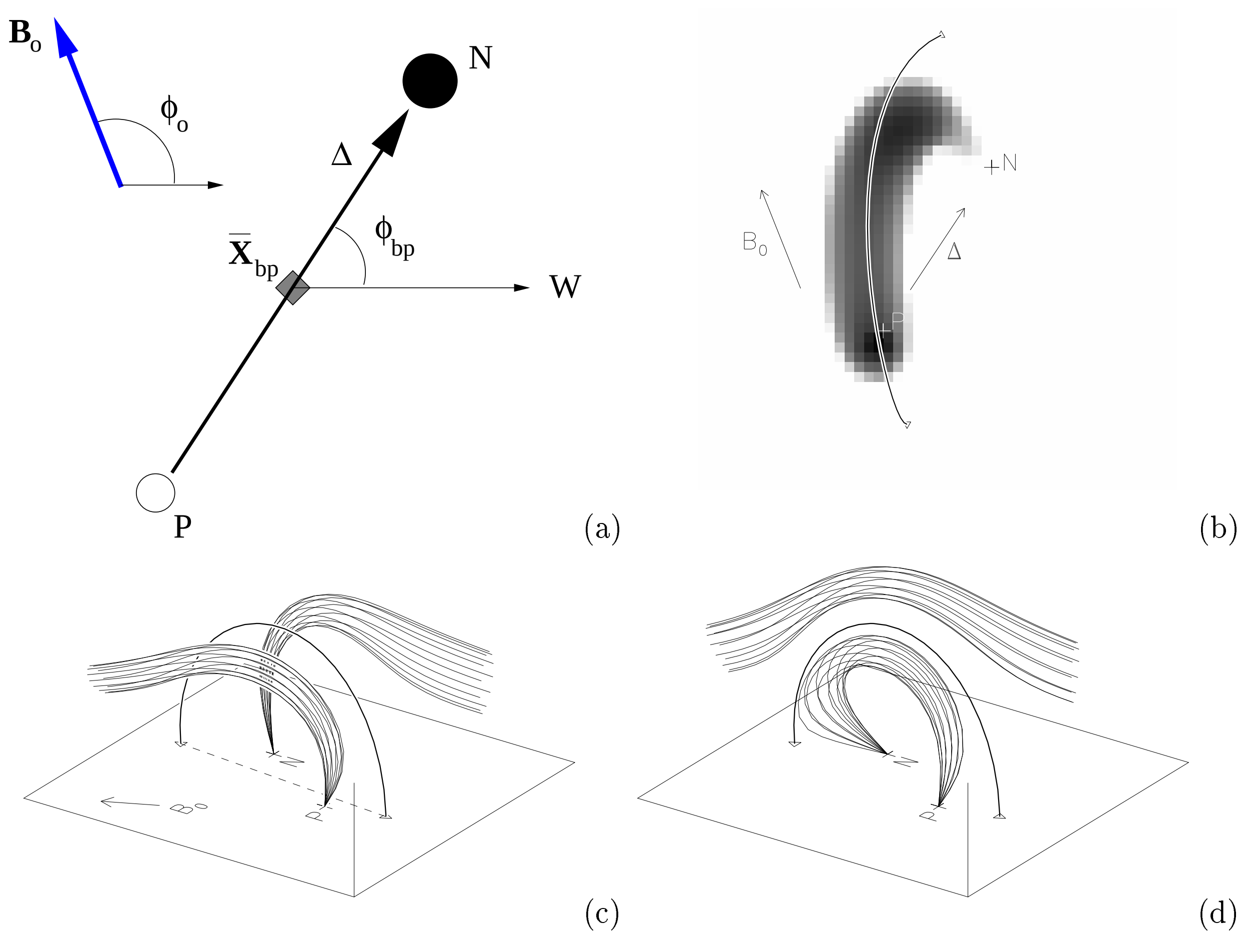

Fig. 1.—. The MCC model of an XBP. (a) The geometry of a bipole and the background field $\mathbf{B}_0$. (b) Emission from flux tube after reconnection. The solid curve shows the separator, arrows indicate the direction of the bipole $\mathbf{\Delta}$ and the background field $\mathbf{B}_0$. (c) Some field lines connecting each of the poles to the background field. The separator is shown as a thick curve. The direction of the background field is indicated by an arrow on the photospheric surface. (d) Field lines after reconnection, including flux inside the separator which connect P to N. This is the flux tube shown in (b).

themselves are unimportant. This is a bold assumption which eliminates, for instance, line-tying of footpoints within a given source. Perhaps the main motivation for this assumption is that magnetograms provide little or no information about line-tying within the magnetic sources themselves. We further assume that the coronal fields remain close to equilibrium, so the magnetic evolution is quasi-static. This common assumption neglects possible energetic contributions from Alfvén waves propagating from the photosphere.

Two poles without internal structure are characterized by four parameters: Φ_+, Φ_-, d, $\phi_{\rm bp}$. The uniform horizontal background field is described by two others: B_0 and ϕ_0. The MCC model yields predictions in terms of these six quantities and their time derivatives. For instance, the minimum interaction distance between the poles must scale as $D \sim \sqrt{\Phi/B_0}$ where Φ is a flux characteristic of Φ_+ and Φ_-. In cases of greatly mismatched fluxes, it seems likely that the interaction distance will depend on the larger pole (Longcope & Kankelborg 1999), so

$$D \ \sim \ \sqrt{\frac{\Phi_>}{B_0}} \quad , \tag{1}$$

where $\Phi_> \equiv \max(\Phi_+, \Phi_-)$. The constant of proportionality will depend on the angle $\phi_{\rm bp} - \phi_0$ between the bipole and the background.

As long as the poles move, but do not change their fluxes, power from a quasi-static model must be linear in photospheric velocity (Longcope & Kankelborg 1999). The velocity $\mathbf{v}_{\rm rel} = d\mathbf{\Delta}/dt$ in this model is the time-derivative of the separation vector. The electromagnetic power must scale as $P \sim |\mathbf{v}_{\rm rel}|\Phi B_0$ where Φ is a combination of Φ_+ and Φ_-, possibly different from that in D. A more detailed model (Longcope & Kankelborg 1999) shows that

$$P \ \sim \ |\mathbf{v}_{\rm rel}|\Phi_< B_0 \quad , \tag{2}$$

where $\Phi_<$ is the smaller of the poles. Considering the limit $\Phi_< \rightarrow 0$, where one poles becomes a "ghost", the liberated power should clearly vanish, as it does in (2).

Since the XBP is powered by reconnection, the post-reconnection loops should be the most visible ones. For bipole convergence, one of the post-reconnection loops connects P to N as shown in fig. 1c. The most recently reconnected flux will be closest to the separator, where the reconnection actually occurred. We expect this most recently reconnected flux to be the brightest and to therefore define the morphology of the XBP, as shown in fig. 1b. In this case the XBP loop will be oriented in a direction intermediate between the bipole ($\mathbf{\Delta}$) and the background ($\mathbf{B}_0$); i.e. at an angle between $\phi_{\rm bp}$ and ϕ_0.

3. The archival survey

We apply the model above to a survey of XBPs and magnetic bipoles from archival SOHO data. Our survey contains 764 different XBPs from 11 *disk surveys*. Each disk survey constitutes a single solar snapshot, including EUV data from full-disk EIT images at both 195 Å and 171 Å and two or more full-disk MDI magnetograms. To minimize effects of time variability the EUV images are separated by less than thirty minutes. All XBPs are identified using the 195 Å which is therefore called the *primary image*. At least one magnetogram must be from a time not longer than one hour from the primary (195Å) image. This magnetogram is used to measure properties of the bipole (Φ_+, Φ_- etc.), while the remaining magnetograms define the velocities of each pole. The EIT and MDI images are all co-aligned using the provided header information. While this alignment information is imperfect, we have found it sufficient for our purpose.

A disk survey is assembled by visually identifying XBPs in the primary (195Å) EIT image. The image contrast is enhanced in order to help with this visual identification, however, this enhancement has no effect on the measurements. A perimeter curve completely enclosing the XBP is traced with the cursor. This perimeter is mapped to each of the other images; this mapping accounts for solar rotation. If necessary, the original perimeter is manually readjusted in order to enclose the XBP in 171 Å, and to completely enclose all obviously relevant poles in every magnetogram (see fig. 2). This is repeated for each XBP identified in the primary image. XBPs closer to disk center are sought preferentially. Analysis of the final results suggest that XBPs away from disk center have been systematically under-sampled in each disk survey.

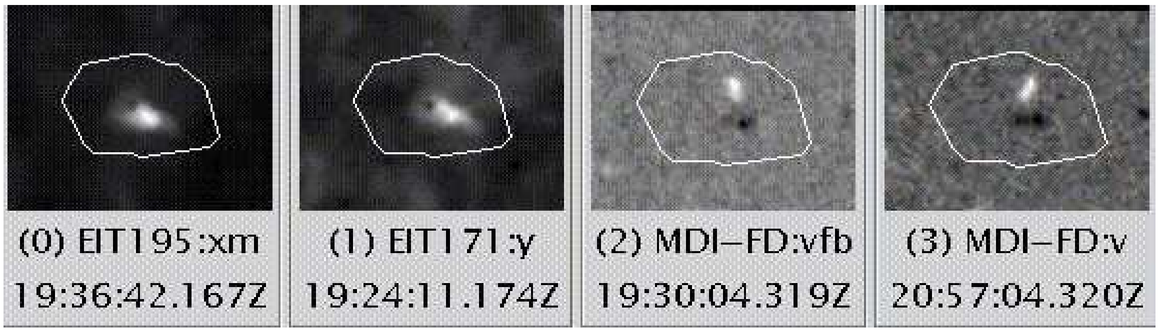

Fig. 2.—. An example of an XBP identified in 195 Å. The four panels shows a small subsection of 195 Å, 171 Å, and two MDI magnetograms (from left to right). A perimeter (thin lines) traced on the 195 Å image is mapped to all other images. This is XBP 5 from disk survey 7.

The eleven disk surveys, summarized in table 1, cover the period between May 1996 and June 1998, within the increasing phase of cycle 23. Each disk survey contains between

Disk survey		EIT data		MDI data			XBPs	
#	date	195Å	171Å	bipole	velocity		found	analyzed
1	1996-05-01	01:29	01:01	01:04	23:28*	—	68	29
2	1996-09-23	01:19	01:00	01:20	02:00	02:58	91	30
3	1997-04-12	07:13	07:00	07:16	07:34	08:02	43	16
4	1997-06-13	19:12	19:00	19:12	20:48	—	70	19
5	1997-08-01	07:12	07:00	06:27	01:36	14:27	54	32
6	1997-10-03	07:12	07:00	07:12	05:58	07:58	80	34
7	1997-11-11	19:36	19:24	19:30	20:57	—	71	31
8	1998-01-01	16:53	16:41	16:00	14:24	—	81	16
9	1998-03-07	01:54	01:40	01:36	03:12	—	79	30
10	1998-04-20	07:25	07:10	07:26	06:06	—	62	19
11	1998-06-06	19:16	19:02	19:12	20:48	—	65	29
	total						764	285

Table 1:. The 11 disk surveys composing the complete archival survey.

*Time on previous day

43 and 91 different XBPs. There is no chance of a single XBP reappearing in two successive disk surveys, since successive surveys are separated by more than a month, while XBP lifetimes never exceed a few days (Golub et al. 1974). Finally, we assume that the XBP population is statistically steady over the survey period, and therefore that all XBPs from the different disk surveys are drawn from a single parent distribution. This assumption permits us to combine our disk surveys into a single survey containing 764 XBPs.

For comparison to other surveys we compute the density of XBPs in our survey. The cumulative histogram in fig. 3 shows the number of XBPs within a given radius from disk center. Near disk center the histogram is consistent with a uniform coverage of 1.1×10^{-4} per square Mm per disk survey. The histogram falls off beyond 20°, suggesting less efficient sampling away from disk center. Furthermore, blind repetition of some disk surveys suggests at least a 20% under-counting near disk center. Correcting for this under-counting gives a central density of $1.3 \times 10^{-4}\,\mathrm{Mm}^{-2}$. Extending this disk-center density to the entire visible hemisphere gives 396 XBPs, of which only 10% to 25% seem the be found in our disk surveys. Our estimated density is similar to the 200–600 XBPs per-disk (0.6×10^{-4}–$2 \times 10^{-4}\,\mathrm{Mm}^{-2}$) found by Golub et al. (1976) in Skylab data. It should be noted, however, that ours was not designed as a statistically complete survey, or to account in any way for the fraction of disk covered by active regions.

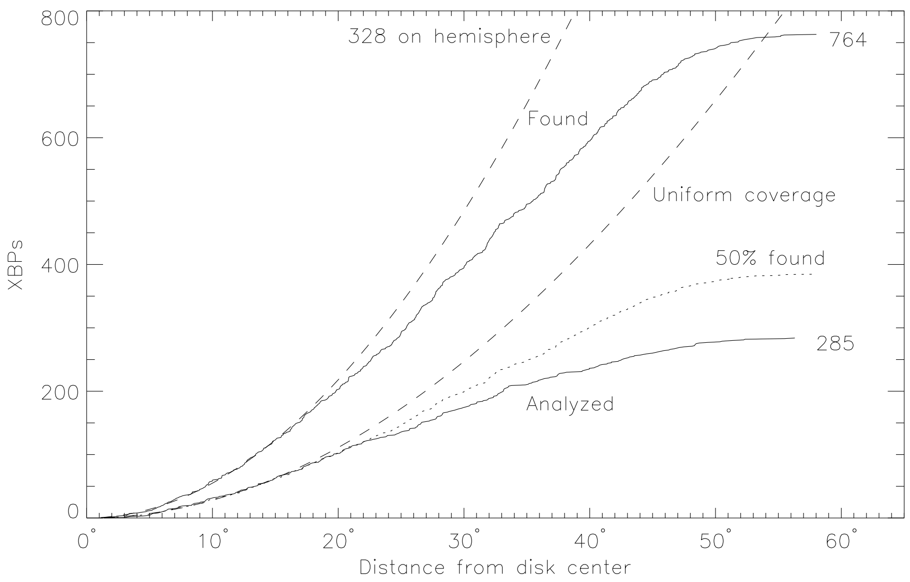

Fig. 3.—. Cumulative histogram of XBPs from the 11 disk surveys versus their distance from disk center (upper solid curve). This approximates a uniform distribution (upper dashed curve) near disk center, and falls off toward the limb. The distribution of XBPs in the analytic survey (lower solid line) is close to 50% of all XBPs found (dotted line) close to disk center.

4. Extracting numbers

The XBPs are quantified in terms of parameters relevant to the MCC reconnection model. Those cases from which all model parameters may be accurately measured, comprise a subset of the original survey which we call the *analytic survey*. XBPs are rejected from the analytic survey if the image in either EUV wavelength is multi-lobed or more complex than a single loop might produce. They are also rejected if the magnetogram images lack one polarity or contain more than a single significant pole of either polarity. The analytic survey contains 285 of the 764 original XBPs. The acceptance rate is about 50% close to disk-center and decreases toward the limb (see fig. 3).

4.1. The coronal loop

The coronal loop, which is the XBP itself, is parameterized from the EUV images inside the traced perimeter. For each EUV wavelength the local background is modeled according to an algorithm developed by Kankelborg et al. (1997), using the brightness at the perimeter. The model background is subtracted and both background-subtracted

(BGS) images are then used to quantify relevant properties of the coronal loop, including its morphology and its total heating power. The integrated BGS emission constitutes a small fraction of the total, typically 10% to 25%.

The loop morphology is parameterized by its location, its length and its orientation, in the primary (195 Å) image. The set of pixels whose BGS intensity exceed half the maximum is used to define the *shape* S of the loop (see fig. 4). The loop location is defined as its center-of-figure

$$\bar{\mathbf{x}}_{\rm euv} \equiv \frac{1}{N}\sum_{i\in S}\mathbf{x}_i \quad , \tag{3}$$

where N is the number of pixels in S, and $\mathbf{x}_i = (x_i, y_i)$ is the location of pixel i. Length and orientation are found from the second moment matrix of S

$$M_{xx} = \frac{1}{N}\sum_{i\in S}(x_i - \bar{x}_{\rm euv})(x_i - \bar{x}_{\rm euv}) \quad , \tag{4}$$

$$M_{xy} = M_{yx} = \frac{1}{N}\sum_{i\in S}(y_i - \bar{y}_{\rm euv})(x_i - \bar{x}_{\rm euv}) \quad , \tag{5}$$

$$M_{yy} = \frac{1}{N}\sum_{i\in S}(y_i - \bar{y}_{\rm euv})(y_i - \bar{y}_{\rm euv}) \quad . \tag{6}$$

The matrix M is transformed to the tangent plane at the heliographic position of pixel $\bar{\mathbf{x}}_{\rm euv}$, yielding M'. The major axis of the equivalent ellipse (that having the same moment matrix M') defines the length $L_{\rm euv}$ and orientation $\phi_{\rm euv}$ of the loop. Given its definition the length $L_{\rm euv}$ naturally refers to a distance on the solar surface. The angle ϕ, in the range $-90°, 90°$, refers to angle North of heliographic West.

There are many potential sources of error in measuring the orientation angle $\phi_{\rm euv}$. To begin with, even ideal coronal loops cannot be unambiguously characterized by a direction, since they are not perfectly straight (see fig. 1b). EUV emission comes from $\sim 10^6$ K plasma, probably near the loop's top, so $\phi_{\rm euv}$ is likely to reflect the loop's direction there. There is further potential for error in identifying the major axis of an ellipse, especially one with small eccentricity. We therefore define the error $\Delta\phi_{\rm euv}$ as the angle at which the ellipse crosses a circle with radius 90% of the semi-major axis (see fig. 4a). Experience has shown that this empirically defined range of angles, $\phi_{\rm euv} - \Delta\phi_{\rm euv} \rightarrow \phi_{\rm euv} + \Delta\phi_{\rm euv}$, does typically include all of the possible orientations suggested by an image.

The total fluxes in BGS images, F_{171} and F_{195}, are used to calculate the loop's peak temperature, $T_{\rm max}$, and emission measure EM. The EIT response to a homogeneous, isothermal plasma is derived using standard EIT software for a plasma of density $n_e = 10^9$ cm^{-3}, using the coronal abundances of Feldman (1992) and the ionization balance of Arnaud and Rothenflug (1985). Using a simple constant-pressure loop model (Rosner,

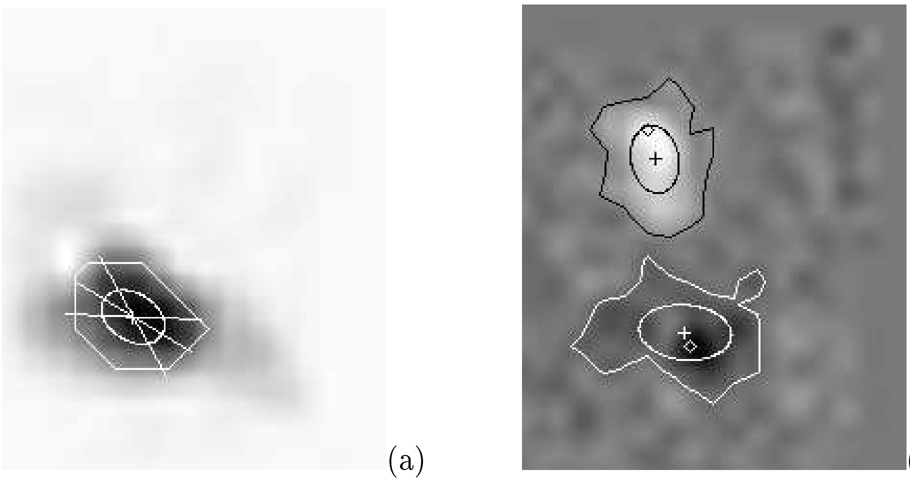

(a) (b)

Fig. 4.—. An example of parameters calculated from an XBP/bipole pair: XBP 5 from disk survey 7. (a) The BGS 195 Å image in reversed grey-scale. The polygon traces regions S, for which $\bar{\mathbf{x}}_{\rm euv} \rightarrow 3.^{\circ}3$N, $28.^{\circ}4$E. The ellipse shown is a one-half sized version of the equivalent ellipse. The center line is $L_{\rm euv} = 8.7 \times 10^8$ cm oriented at $\phi_{\rm euv} = -44^{\circ}$. It is flanked by lines differing in angle by the error $\Delta\phi_{\rm euv} = 31^{\circ}$. (b) The MDI image with contours at ± 20 G (angular lines) and half-sized equivalent ellipses for each pole. Diamonds mark the maximum and minimum pixels; pluses mark the flux-weighted centers $\mathbf{x}_{\pm}$ from which it follows that $\bar{\mathbf{x}}_{\rm bp} \rightarrow 3.^{\circ}7$N, $28.^{\circ}3$E (rotated to the time of the primary image), $L_{\rm bp} = 1.1 \times 10^9$ cm and $\phi_{\rm bp} = -77^{\circ}$. The error in angle is $\Delta\phi_{\rm bp} = 38^{\circ}$

Tucker, & Vaiana 1978, Serio et al. 1981) in conjunction with these EIT responses, we calculated modified response curves in data numbers (DN) per unit emission measure with $T_{\rm max}$ as the independent variable. The resulting integrated response of EIT to coronal loops is shown in fig. 5 along with the isothermal repsonses. The integrated loop response has a large tail at high $T_{\rm max}$ because hot loops include cool footpoints.

The temperature is then found from the flux ratio

$$T_{\rm max} = 10^{6.3}\left(\frac{F_{195}}{F_{171}}\right) \quad , \quad 0.9\,{\rm MK} < T_{\rm max} < 1.6\,{\rm MK} \quad , \tag{7}$$

which is independent of the choice of filter combination to high accuracy. For higher temperatures the filter ratio remains approximately constant at 0.5. We use equation (7) to assign temperatures in the specified range to all of the observed loops. The emission measure of the unresolved loop is then estimated using a linear combination that yields an approximately flat response over the specified temperature range:

$$EM = 1.4 \times 10^{43}\,{\rm cm}^{-3}\,(\,F_{171} - 0.4F_{195}\,) \pm 19\% \quad . \tag{8}$$

(This is valid for EIT's "clear" filter; fluxes obtained with other filters are rescaled to clear filter values during data preparation.) Using the loop scaling laws (Serio et al. 1981) the

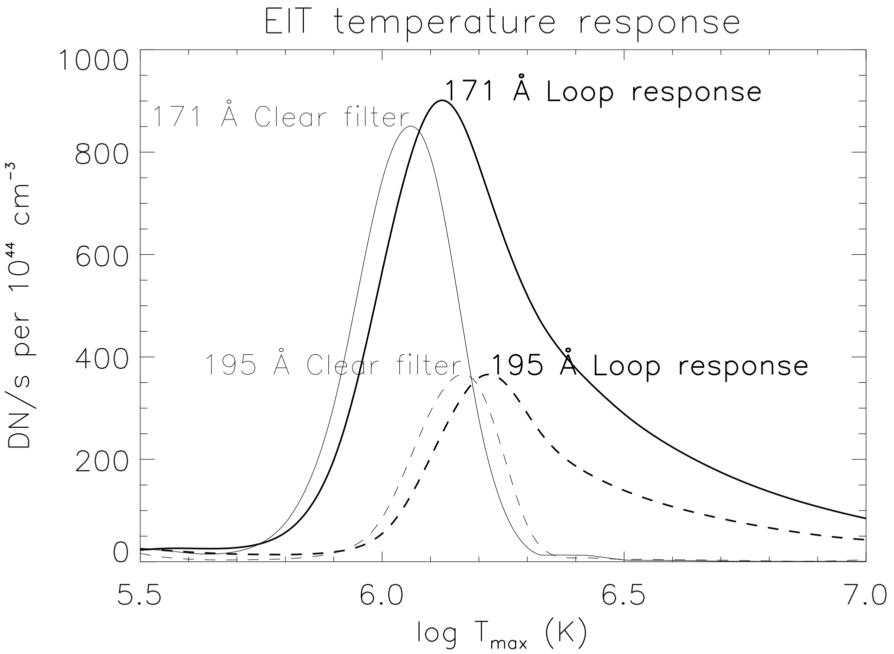

Fig. 5.—. The EIT responses at 171Å and 195Å to an isothermal plasma and the integrated loop response at the same two wavelengths to loops of varying apex temperature $T_{\rm max}$. Solid and dashed curves show 171Å and 195Å responses respectively

total power heating the unresolved loop is

$$P = 1.3 \times 10^{-19}\, EM\, T_{\rm max}^{-1/2} \quad , \tag{9}$$

in ergs/sec. The power P is therefore identified with the power input attributable reconnection.

4.2. The bipole

The positive and negative poles are defined as the largest contiguous regions above $B = 20$ G and below -20 G respectively (see fig. 4b). To be acceptable each pole must also contain the extremal pixel for the entire sub-image. The total flux in each region $\Phi_{\pm}$ is the flux of the pole, corrected for viewing angle by assuming purely radial field. This value is likely to underestimate the true flux since the region excludes line-of-sight field strengths below 20 G. The field-strength-weighted center-of-flux for each pole defines its location $\mathbf{x}_{\pm}$. Errors in each location are estimated using the second flux-weighted moment matrix, projected onto the tangent plane.

The location of the bipole is defined by the midpoint

$$\bar{\mathbf{x}}_{\rm bp} \;\equiv\; \tfrac{1}{2}(\mathbf{x}_{+} + \mathbf{x}_{-}) \quad . \tag{10}$$

The bipole orientation $\mathbf{\Delta}$ points from the positive to negative pole

$$\mathbf{\Delta} \;=\; \mathbf{x}_{-} - \mathbf{x}_{+} \quad . \tag{11}$$

This vector is projected onto the tangent plane at the heliographic location of $\bar{\mathbf{x}}_{\rm bp}$ to yield $\mathbf{\Delta}'$, whose length $L_{\rm bp}$ and orientation angle $\phi_{\rm bp}$ parameterize the bipole. The angle is once again defined from heliographic West, but ranges from -180° to 180°.

Magnetograms from times t_1 and t_2 can be used to find the relative velocity

$$\mathbf{v}_{\rm rel} \;=\; \frac{\mathbf{\Delta}'_2 - \mathbf{\Delta}'_1}{t_2 - t_1} \quad . \tag{12}$$

Accurate co-alignment of the magnetograms to the EUV images is irrelevant since the velocity refers to a change in $\mathbf{\Delta}'$. If more than two magnetograms exist, eq. (12), is replaced with a least-squares fit. Each component of $\mathbf{\Delta}'_k$ is fit to a line, the slope of which defines that component of $\mathbf{v}_{\rm rel}$.

5. Results

The data analysis described above was performed on all 285 XBP/bipole pairs in the analytic survey. The resulting dataset provides evidence in favor of the MCC model and against the naive bipole model. It also provides several consistency checks, testing the survey's underlying assumptions.

5.1. Sizes

The survey contains bipoles and XBPs whose sizes range between 4 and 40 Mm. It is likely that the lower bound reflects the spatial resolution of the data. Plotting the pole separation $L_{\rm bp}$ versus XBP length $L_{\rm euv}$ (fig. 6a) reveals that the two are unquestionably correlated (Spearman's $r_s = 0.53$ [Press et al. 1986]). This provides a somewhat trivial consistency check, confirming that the XBP and bipole are related to one another.

A more significant statement may be made from the 37% of cases where the XBP is longer than the bipole ($L_{\rm bp} < L_{\rm euv}$). While these are not a majority, their very existence weighs in favor of the MCC and against the naive bipole model. Under the naive bipole model the magnetic poles form the endpoints of the loop. Under this hypothesis it is difficult to envision the loop appearing longer than the distance between the poles it connects. On the other hand, the separator field line, which defines the XBP in the MCC model, can be either longer or shorter than the bipole depending on the angle of the background field (i.e. $\phi_{\rm bp} - \phi_0$).

According to the MCC, a necessary condition for reconnection is that the poles be separated by *less than* the interaction distance D. Ignoring the angle dependence in D and taking the constant of proportionality as unity, the necessary condition for an XBP can be written

$$L_{\rm bp} \ \le \ D \ = \ \sqrt{\frac{\Phi_>}{B_0}} \ \ , \tag{13}$$

where B_0 is the strength of the background field overlying the XBP in question. Plotting the bipole separation versus the maximum flux $\Phi_>$ (fig. 6b) provides a test of this condition. Initial support can be found in the clear correlation between $\Phi_>$ and $L_{\rm bp}$ (Spearman's $r_s = 0.33$). Furthermore, dotted lines representing (13) for choices of B_0 follow the data's trend. Detailed analysis reveals that eq. (13) is satisfied for 95% of all bipoles with $B_0 = 3.2$ G and for 80% with $B_0 = 5.6$ G. Either of these might be taken as plausible measurements of the "typical" B_0. The cases violating (13), 5% or 20% respectively, can be attributed to a favorable alignment of the background field ($|\phi_0 - \phi_{\rm bp}| \gtrsim 120°$) or to a local value of B_0

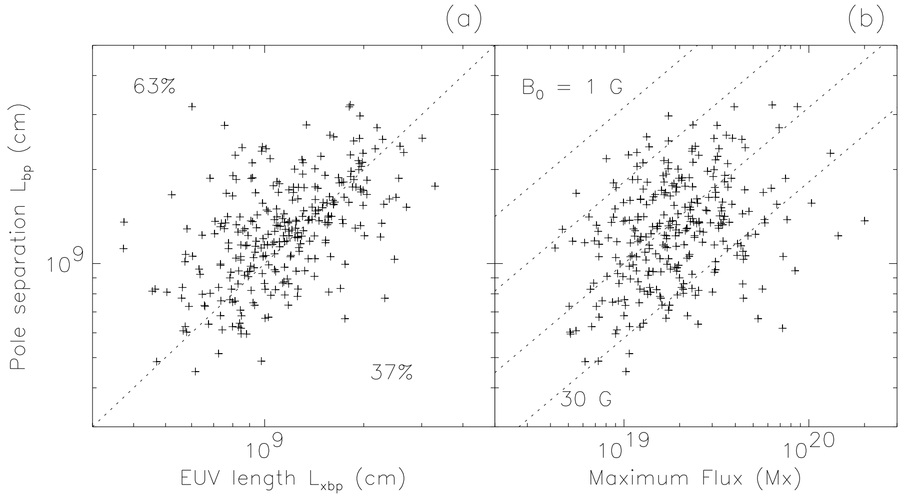

Fig. 6.—. Scatter plots of lengths. (a) $L_{\rm bp}$ versus $L_{\rm euv}$. 63% of the points lie above the diagonal (dotted line); these points have $L_{\rm euv} < L_{\rm bp}$. (b) $L_{\rm bp}$ versus $\Phi_>$. Dotted lines shows the nominal interaction distance $\sqrt{\Phi_>/B_0}$ for cases $B_0 = 1$ G (top line), 3 G, 10 G, and 30 G (bottom line).

smaller than typical.

5.2. Magnetic fluxes

The fluxes $\Phi_\pm$ in our survey are distributed approximately log-normally with median 1.3×10^{19} Mx in each case. This median is similar to the value 2×10^{19} Mx found by Golub et al. (1977) from Kitt Peak measurements of bipoles beneath Skylab XBPs.

A scatter plot of Φ_- versus Φ_+ (fig. 7) can be used to shed light on the process underlying their interaction. Chance collisions between previously unrelated poles would produce bipoles where Φ_+ and Φ_- were completely uncorrelated in a rank-order sense. Figure 7 reveals, to the contrary, that positive and negative fluxes within a bipole are significantly correlated. The measured value of Spearman correlation coefficient, $r_s = 0.33$, is consistent with a population of XBPs in which only 67% are chance collisions between unrelated poles, while the remaining 33% involve bipoles where where $\Phi_+ \simeq \Phi_-$, for instance from emergence. This result is consistent with the study of Harvey (1985), who found that one-third of all He λ10830 dark points (a proxy for XBPs) were associated with flux emergence, and with the study of Webb et al. (1993) who found that 7 of 25 (28%) of XBPs were associated with emerging flux.

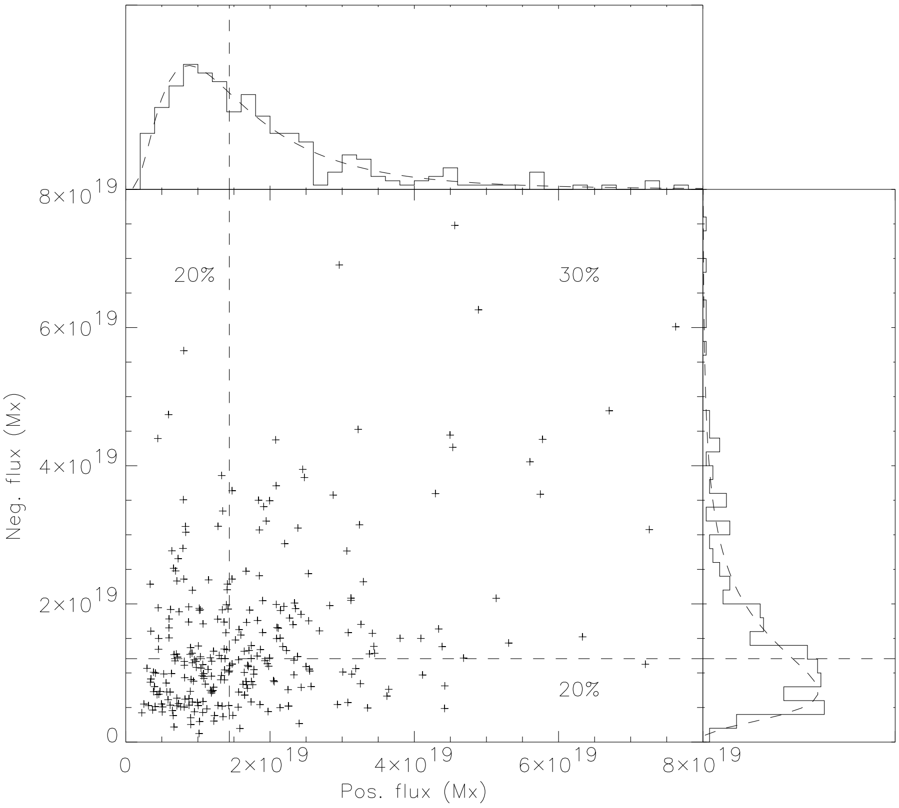

Fig. 7.—. A scatter plot of Φ_- versus Φ_+ marked with pluses. Histograms of each quantity are plotted along its axis, along with a fit to a log-normal distribution (dashed). The medians are shown with dashed lines. Fractions in each of the quadrants are indicated.

5.3. Orientation

Neither the bipoles nor the XBPs show a preferred orientation on the solar disk. The values of $\phi_{\rm bp}$ and $\phi_{\rm euv}$ show no correlation with heliographic latitude, as shown in fig. 8 ($r_s = 0.008$ and $r_s = -0.08$ respectively). Furthermore, histograms are statistically consistent with a uniform distribution in each case. This result forms a natural extension of the fact that magnetic bipoles adhere less closely to Hale's polarity law the smaller they are.

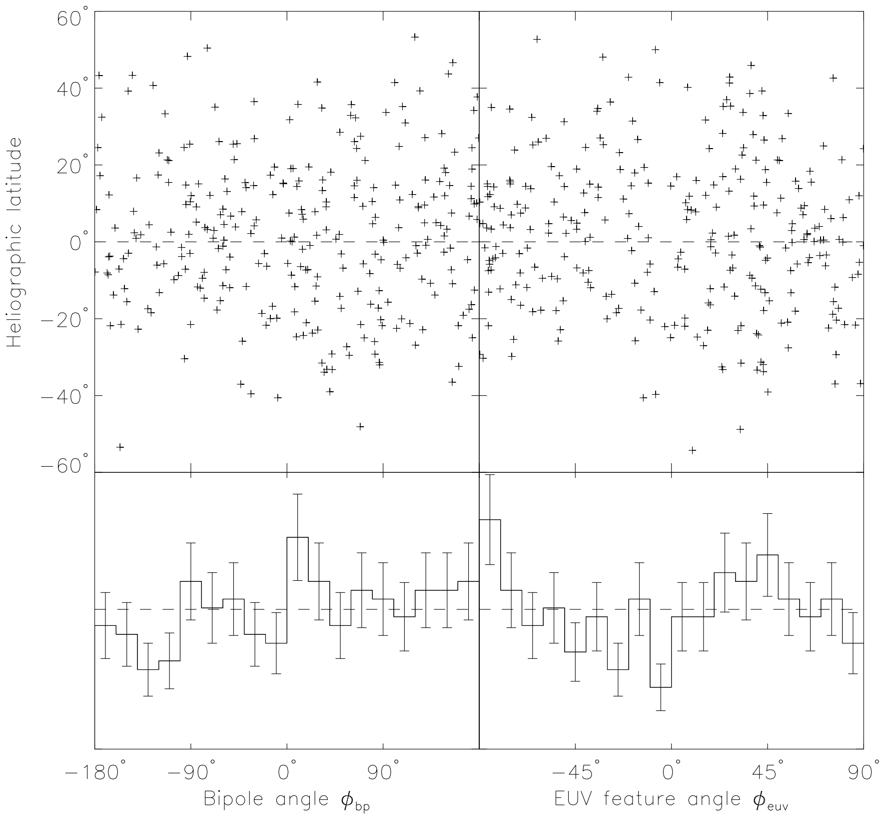

Fig. 8.—. Scatter plots of latitude versus orientation angle for both bipoles and XBPs. Lower panels show histograms of $\phi_{\rm bp}$ and $\phi_{\rm euv}$, compared to a uniform distribution of angles (dashed line).

A test of the MCC versus the naive bipole hypothesis is to be found in the angle by which the bipole and XBP are misaligned,

$$\delta\phi \ \equiv \ \phi_{\rm bp} - \phi_{\rm euv} \quad . \tag{14}$$

According to the MCC, $\phi_{\rm euv}$ will be intermediate between $\phi_{\rm bp}$ and ϕ_0, the angle of the background field. Without a measurement of ϕ_0, it is still possible to establish that $\delta\phi \neq 0$, and thus that the bipole and the XBP are oriented in different directions. Under the naive bipole model it is difficult to envision misalignment above the level of measurement error,

$$\sigma_\phi \;=\; \sqrt{\Delta\phi_{\rm euv}^2 + \Delta\phi_{\rm bp}^2} \quad . \tag{15}$$

Figure 9 shows the misalignment angles $\delta\phi$ for all 154 of the XBP/bipole pairs with well determined axes: $\sigma_\phi < 30^\circ$. Misalignments greater than σ_ϕ occur in 72 of these, and the χ^2 statistic

$$\chi^2 = \sum_i \left(\frac{\delta\phi_i}{\sigma_{\phi,i}}\right)^2 \quad , \tag{16}$$

is 469.5 for the 154 points. This completely rules out a version of the naive model in which $\delta\phi$ is distributed about zero due to Gaussian measurement errors.

Twisted flux within the bipole itself might provide an alternative explanation for a misalignment angle $\delta\phi$ in the spirit of the naive model. Previous investigation of active region loops show definite tilts relative to the magnetic axis as a result of directly measured currents (Pevtsov, Canfield, & McClymont 1997). Without well resolved vector magnetic measurements of each pole it is not possible to test this hypothesis directly. In active regions, however, both the sense of current and the misalignment angle are correlated with latitude (Pevtsov, Canfield, & Metcalf 1995). For our XBP survey $\delta\phi$ shows no significant correlation with latitude (see fig. 9). The Northern hemisphere contains an excess of positively aligned bipoles, but this excess is not quite statistically significant in our data.

5.4. Heating power

Calculated heating powers in our survey are distributed approximately log-normally with a median value $P = 1.0 \times 10^{24}$ erg/sec and a mean of $\bar{P} = 1.5 \times 10^{24}$ erg/sec. The power is well correlated with the minimum flux $\Phi_<$ and the loop's apparent length $L_{\rm euv}$ (see fig. 10, $r_s = 0.32$ and 0.24 respectively). These correlations are consistent with the predictions of the reconnection model.

Due to large errors in the velocity measurements it was not possible to make more direct comparisons to the prediction. According to the reconnection hypothesis the dissipated power is $P = \Phi_< B_0 |\mathbf{v}_{\rm rel}|$. This agrees with the observed median $P = 10^{24}$ erg/sec for a very reasonable photospheric velocity of $|\mathbf{v}_{\rm rel}| = 150$ m/sec combined with the median flux $\Phi = 1.3 \times 10^{19}$ Mx and the background field strength $B_0 \simeq 5\,$G found using loop lengths.

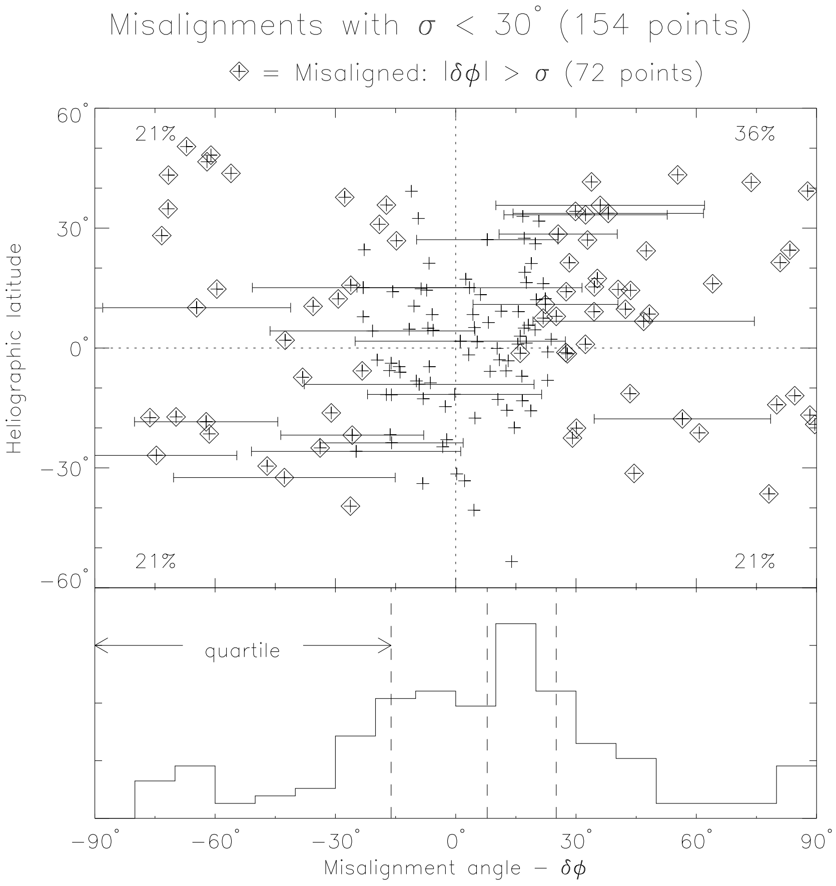

Fig. 9.—. A scatter plot of solar latitude versus misalignment angle $\delta\phi$ for those cases where $\sigma_\phi < 30°$. Error bars show σ_ϕ on a random set of points. Points misaligned beyond measurement error ($|\delta\phi > \sigma_\phi$) are marked with diamonds. The lower panel shows a histogram of $\delta\phi$.

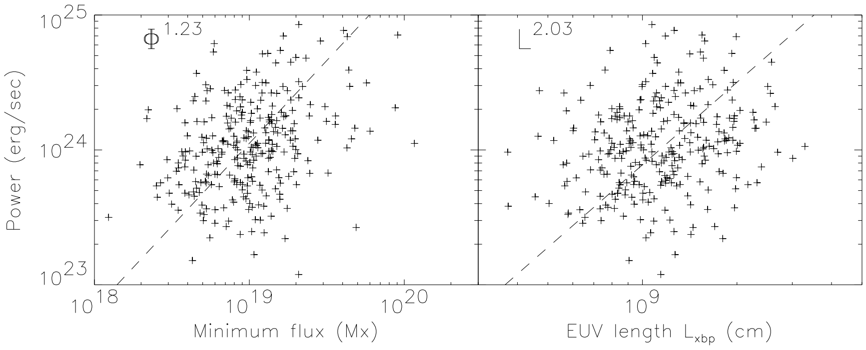

Fig. 10.—. Scatter plots of calculated heating power P versus $\Phi_<$ (left) and $L_{\rm euv}$ (right).

This inferred velocity is in good agreement with other measurements of the motions of small magnetic elements in the quiet Sun (Schrijver et al. 1996).

6. Discussion

We have found, in a survey of X-ray bright point observations, support for the hypothesis that these coronal features are powered by magnetic reconnection. In particular, the reconnection hypothesis fits the observations better than the naive bipole hypothesis, whereby no part of the magnetic bipole is heated preferentially. The observed coronal loop is often quantitatively different from the bipole itself; it is physically longer and oriented in a different direction. This is a natural consequence of the reconnection hypothesis, but would be less natural under the naive bipole hypothesis. The separation between poles scales with flux in a manner consitent with magnetic reconnection in three dimensions.

The survey has also provided some quantitative information about reconnection in the quiet Sun. The relationship between length and magnetic flux suggests that most XBPs occur in a horizontal background field of 3–6 Gauss. The degree of correlation between the magnetic fluxes suggests that one-third of XBPs occur from emergence of small flux loops while two-thirds are due to random collision. This conclusion was reached without direct observation of the converging or diverging motions of the elements.

This work was supported by NASA grant NAG5-7296.

References

Arnaud, M., & Rothenflug, R. 1985, Astron. Astrophys. Suppl. Ser., 60, 425

Delaboudiniere, J.-P., et al. 1995, Solar Phys., 162, 291

Feldman, U. 1992, Physica Scripta, 46, 202

Fisher, G., & Hawley, S. 1990, ApJ, 357, 243

Golub, L., Krieger, A. S., Harvey, J. W., & Vaiana, G. S. 1977, Solar Phys., 53, 111

Golub, L., Krieger, A. S., Silk, J. K., Timothy, A. F., & Vaiana, G. S. 1974, ApJ, 189, L93

Golub, L., Krieger, A. S., & Vaiana, G. S. 1976, Solar Phys., 50, 311

Habbal, S. R., Dowdy, J., J. F., & Withbroe, G. L. 1990, ApJ, 352, 333

Habbal, S. R., & Withbroe, G. L. 1981, Solar Phys., 69, 77

Harvey, K. L. 1985, Australian J. Phys., 38, 875

Harvey, K. L., Jones, H. P., Schrijver, C. J., & Penn, M. J. 1999, Solar Phys., 190, 35

Harvey, K. L., Nitta, N., Strong, K. T., & Tsuneta, S. 1994, in X-ray solar physics from Yohkoh, ed. Y. Uchida, T. Watanabe, K. Shibata, & H. S. Hudson (Universal Academy Press), 21

Kankelborg, C. C., Walker, A. B. C., II, & Hoover, R. B. 1997, ApJ, 491, 952

Kankelborg, C. C., Walker, A. B. C., II, Hoover, R. B., & Barbee, J., T. W. 1996, ApJ, 466, 529

Krieger, A. S., Vaiana, G. S., & van Speybroeck, L. P. 1971, in Solar Magnetic Fields, ed. R. Howard (IAU), 397

Longcope, D. W. 1998, ApJ, 507, 433

Longcope, D. W., & Kankelborg, C. C. 1999, ApJ, 524, 483

Longcope, D. W., & Silva, A. V. R. 1998, Solar Phys., 179, 349

Nolte, J. R., Solodyna, C. V., & Gerassimenko, M. 1979, Solar Phys., 63, 113

Parnell, C. E., Priest, E. R., & Golub, L. 1994, Solar Phys., 151, 57

Pevtsov, A. A., Canfield, R. C., & McClymont, A. N. 1997, ApJ, 481, 973

Pevtsov, A. A., Canfield, R. C., & Metcalf, T. R. 1995, ApJ, 440, L109

Press, W. H., Flannery, B. P., Teukolsky, S. A., & Vetterling, W. T. 1986, Numerical Recipes: The art of scientific computing (Cambridge: Cambridge University Press)

Priest, E. R., Parnell, C. E., & Martin, S. F. 1994, ApJ, 427, 459

Rosner, R., Tucker, W. H., & Vaiana, G. S. 1978, ApJ, 220, 643

Scherrer, P. H., et al. 1995, Solar Phys., 162, 129

Schrijver, C. J., Shine, R. A., Hagenaar, H. J., & Hurlburt, N. 1996, ApJ, 468, 921

Serio, S., Peres, G., Vaiana, G. S., Golub, L., & Rosner, R. 1981, ApJ, 243, 288

Strong, K. T., Harvey, K., Hirayama, T., Nitta, N., Shimizu, T., & Tsuneta, S. 1992, PASJ, 44, L161

Vesecky, J. F., Antiochos, S. K., & Underwood, J. H. 1979, ApJ, 233, 987

Webb, D. F., Martin, S. F., Moses, J. W., & Harvey, J. W. 1993, Solar Phys., 144, 15

This preprint was prepared with the AAS LaTeX macros v4.0.